

Uncertainty Quantification for the Relativistic Inverse Stellar Structure Problem

Lee Lindblom¹ and Tianji Zhou²

¹*Department of Physics, University of California at San Diego, San Diego, California, 92093 USA*

²*Department of Physics and Astronomy, Haverford College, Haverford, Pennsylvania, 19041 USA*

(Dated: February 18, 2025)

The relativistic inverse stellar structure problem determines the equation of state of the stellar matter given a knowledge of suitable macroscopic observable properties (e.g. their masses and radii) of the stars composed of that material. This study determines how accurately this equation of state can be determined using noisy mass and radius observations. The relationship between the size of the observational errors and the accuracy of the inferred equation of state is evaluated, and the optimal number of adjustable equation of state parameters needed to achieve the highest accuracy is determined.

I. INTRODUCTION

The quantity and quality of astrophysical observations of the masses and radii of neutron stars has improved significantly in the past decade [1–9]. Masses have now been measured at the few percent level for dozens of neutron stars, and both mass and radius have been measured for a few neutron stars at the 10-20% level. It is well known that a knowledge of the masses and radii of neutron stars can be used to infer the equation of state of the high density material in the cores of these stars [10]. The purpose of this paper is to apply a simple uncertainty quantification analysis [11] to the relativistic inverse stellar structure problem, i.e. the problem of determining the high density neutron-star equation of state from a knowledge of the masses and radii of those stars. The goal of this analysis is to determine the relationship between the accuracy of the available mass-radius data with the accuracy of the equation of state that can be inferred from those data.

Section II of this paper describes the method of solving the relativistic inverse stellar structure problem used in this study. This method constructs a parametric representation of the high-density equation of state by fixing its parameters to minimize the differences between the resulting model neutron stars and the observed mass-radius data [12–14]. The particular parametric equation of state representation used in this study is a causal spectral representation with basis functions constructed from Chebyshev polynomials [15]. The basic properties of this equation of state representation are summarized in Appendix A.

Section III constructs the collections of mock noisy mass-radius data used in this study to evaluate the accuracy of the equations of state determined from them. These mock noisy data are constructed here by adding random errors of various sizes to the exact masses and radii computed from the GM1L nuclear-theory based neutron-star equation of state [16–18]. Four collections of mock data, each containing 1000 noisy mass-radius curves, are constructed with random fractional error amplitudes 0.1%, 1%, 10%, and 20%.

Section IV solves the relativistic inverse stellar struc-

ture problem using the mock noisy mass-radius data prepared in Sec. III. Parameterized equations of state using different numbers of spectral parameters, $N_{\text{parms}} = 1, \dots, 5$ are determined for each noisy mass-radius curve by solving the inverse stellar structure problem as described in Sec. II. The accuracy of these parametric equations of state are evaluated by measuring the differences between them and the exact GM1L equation of state from which the mock data are constructed. The dependence of these equation of state errors on the accuracy of the mock observational data is then evaluated for equation of state representations with different numbers of spectral parameters.

Section V presents a brief summary of the results of the uncertainty quantification analysis presented in this study, along with a discussion of some interesting implications of these results.

II. INVERSE STELLAR STRUCTURE PROBLEM

The matter in the cores of neutron stars is driven to very high temperatures by the gravitational collapse of the matter that forms these stars. These temperatures briefly become high enough to disrupt the atomic nuclei of this matter, so this material is expected to have universal thermodynamic properties determined by nuclear physics and not on the prior thermodynamic history of material from which it formed. All neutron stars are therefore expected to be composed of material having the same high-density equation of state. The relativistic inverse stellar structure problem determines this equation of state from a knowledge of the macroscopic observable properties of neutron stars, e.g. their masses and radii or tidal deformabilities [14]. This section summarizes the particular solution to this problem used in this study [12, 13].

The relativistic inverse stellar structure problem is solved here by representing the unknown equation of state parametrically, $\epsilon = \epsilon(p, v_a)$, where ϵ is the total energy density of the material, p is the pressure, and the v_a for $a = 1, \dots, N_{\text{parms}}$ are adjustable parameters. These parameters are fixed by making the stellar models

based on this equation of state match the observational mass-radius data $\{M_i, R_i\}$ for $i = 1, \dots, N_{\text{MR}}$ as closely as possible.

The particular equation of state representation used in this study is based on a Chebyshev polynomial spectral expansion [15] which is described in Appendix A. The Oppenheimer-Volkoff relativistic stellar structure equations [19] are solved using the equation of state with specified values of v_a to determine the masses, $M(p_c^i, v_a)$, and radii, $R(p_c^i, v_a)$, of the stellar models with central pressures p_c^i . Given a collection of mass-radius observables, $\{M_i, R_i\}$ for $i = 1, \dots, N_{\text{MR}}$, the values of the equation of state parameters v_a are adjusted to make the stellar model properties $\{M(p_c^i, v_a), R(p_c^i, v_a)\}$ match the observables $\{M_i, R_i\}$ as closely as possible. This is done by minimizing the error function χ^2 , defined by,

$$\chi^2(p_c^i, v_a) = \frac{1}{N_{\text{MR}}} \sum_{j=1}^{N_{\text{MR}}} \left\{ \left[\log \left(\frac{M(p_c^j, v_a)}{M_j} \right) \right]^2 + \left[\log \left(\frac{R(p_c^j, v_a)}{R_j} \right) \right]^2 \right\}, \quad (1)$$

with respect to the equation of state parameters, v_a , as well as the central pressures, p_c^i , of the stars with observational data points, $\{M_i, R_i\}$. The equation of state determined by the parameters v_a that minimize χ^2 is therefore an approximate solution to the inverse stellar structure problem.

The mock observational data points $\{M_i, R_i\}$ used in this study were constructed from a particular nuclear-theory based equation of state. Since the exact equation of state is known in this case, it is possible to evaluate the accuracy of the parametric equation of state, $\epsilon = \epsilon(p, v_a)$, determined by the solution to the inverse stellar structure problem. This is done by evaluating the equation of state error function, Δ , defined by,

$$\Delta^2(v_a) = \frac{1}{N_{\text{EOS}}} \sum_{k=1}^{N_{\text{EOS}}} \left[\log \left(\frac{\epsilon(p_k, v_a)}{\epsilon_k} \right) \right]^2, \quad (2)$$

where $\{\epsilon_k, p_k\}$ are points from the exact equation of state table used to generate the mock observational data points, $\{M_i, R_i\}$. The Chebyshev polynomial based equation of state representations used in this study have been shown to provide convergent representations for a wide range of neutron-star equations of state [15].¹ This study explores the extent to which approximate solutions to the inverse stellar structure problem are also convergent in the sense that they produce equation of state error functions $\Delta(v_a)$ that decrease toward zero as the number of parameters v_a increases.

III. NOISY MASS-RADIUS DATA

Mock noisy observational data $\{M_i, R_i\}$ are constructed for this study by adding random errors to a collection of points $\{\tilde{M}_i, \tilde{R}_i\}$ from the exact mass-radius curve associated with a known equation of state. These random errors are parameterized by an error amplitude \mathcal{A} and a random phase variable δ . The noisy mock data $\{M_i, R_i\}$ are generated from $\{\tilde{M}_i, \tilde{R}_i\}$:

$$M_i = (1 + \delta\mathcal{A}) \tilde{M}_i, \quad (3)$$

$$R_i = (1 + \delta\mathcal{A}) \tilde{R}_i. \quad (4)$$

The random phase variables δ are uniformly distributed over the domain $-1 \leq \delta \leq 1$. They are computed for this study using the random number generator ran2 from Ref. [20]. The error amplitude \mathcal{A} is the maximum fractional error of each point in each noisy mock observational mass-radius curve, $\{M_i, R_i\}$.

The reference equation of state used to compute the mock $\{M_i, R_i\}$ data for this study is the nuclear-theory based equation of state GM1L. This equation of state was constructed in Ref. [16] from the relativistic mean field GM1 equation of state of Ref. [17] by adjusting the slope of the symmetry energy to agree with the established value, $L = 55$ MeV, using the formalism developed in Ref. [18]. The masses and radii of the neutron-star models computed from this equation of state are illustrated in Fig. 1 for the models with masses in the astrophysically interesting range $M \geq 1.2M_{\text{sun}}$.

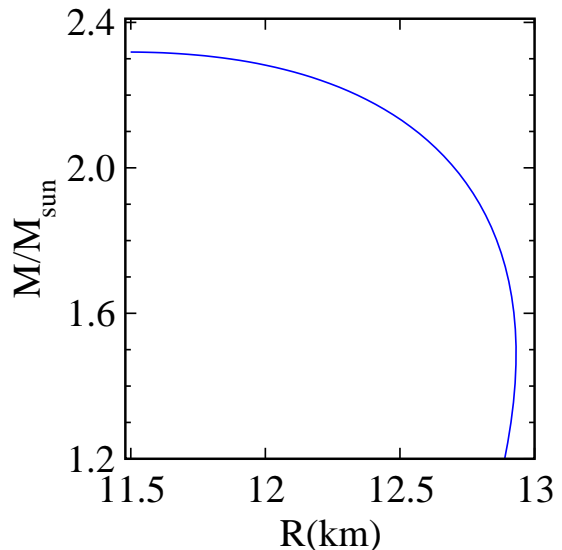


FIG. 1: Neutron-star model masses and radii computed from the GM1L nuclear-theory based equation of state.

The reference $\{\tilde{M}_i, \tilde{R}_i\}$ data points used in this study were selected from the mass-radius curve illustrated in Fig. 1. The number of data points N_{MR} was chosen to be $N_{\text{MR}} = 10$ for this study. This aspirational choice is somewhat larger than the currently available number

¹ The mock mass-radius data analyzed in this study are from the contiguous branch of stable neutron-stars. The Chebyshev based representations have been tested for a wide range of neutron-star equations of state, including those with a range of phase transitions that may exist in these stars.

of high quality data points, but is within the range of what might become available in the not too distant future. The distribution of these $N_{\text{MR}} = 10$ data points are also chosen aspirationally for this study. Rather than choosing these points randomly from the astrophysically relevant range of masses, $1.2M_{\text{sun}} \leq M \leq M_{\text{max}}$, they are chosen here to sample models whose central pressures are relatively uniformly distributed along the high density equation of state curve. Figure 2 illustrates the \tilde{M}_i chosen here as a function of the central pressures of those stellar models. The equation of state errors achieved with these aspirational choices for the mock observational data are likely to be somewhat smaller than could be achieved with a smaller number of randomly distributed data points. The numerical values of these exact $\{\tilde{M}_i, \tilde{R}_i\}$ data points are listed in Table I.

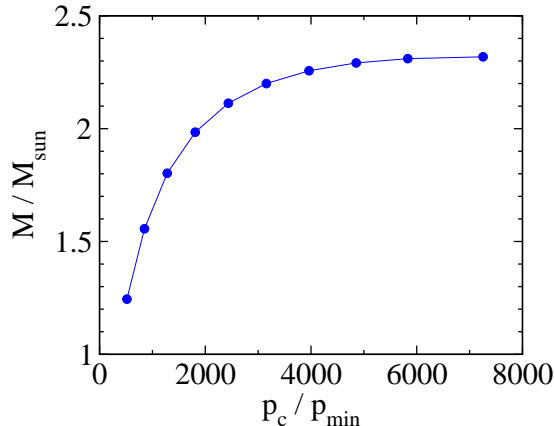


FIG. 2: Neutron-star masses as functions of their central pressures for the ten $\{\tilde{M}_i, \tilde{R}_i\}$ reference data points used in this study. The constant $p_{\text{min}} = 1.20788 \times 10^{32} \text{ erg/cm}^3$ used to scale the pressures in this figure is the lower limit of the domain on which spectral representations are used for the high density equation of state.

TABLE I: $\{\tilde{M}_i, \tilde{R}_i\}$ data for the neutron-star models computed from the GM1L nuclear-theory equation of state. These reference $\{\tilde{M}_i, \tilde{R}_i\}$ values are used to generate the noisy data sets for the uncertainty quantification analysis in this study.

\tilde{M}/M_{sun}	$\tilde{R}(\text{km})$	\tilde{M}/M_{sun}	$\tilde{R}(\text{km})$
1.244629	12.90062	2.200004	12.34184
1.556269	12.92859	2.256765	12.13824
1.802454	12.85875	2.291466	11.93727
1.984403	12.71947	2.310322	11.74336
2.112802	12.54009	2.318418	11.49951

Starting from the exact reference $\{\tilde{M}_i, \tilde{R}_i\}$ given in Table I, collections of noisy mock data $\{M_i, R_i\}$ were constructed using Eqs. (3) and (4) for four different fractional error amplitudes: $\mathcal{A} = \{0.2, 0.1, 0.01, 0.001\}$. The larger values, $\mathcal{A} = \{0.2, 0.1\}$, are more or less at the

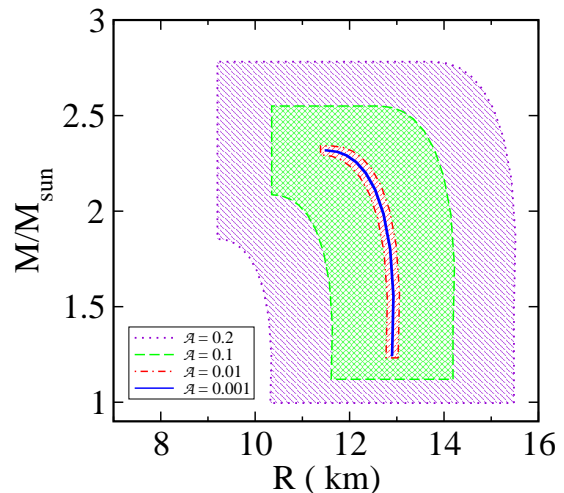


FIG. 3: Regions of the mass-radius plane occupied by the perturbed $\{M_i, R_i\}$ data sets used in this study. Random perturbations with amplitudes $\mathcal{A} = \{0.2, 0.1, 0.01, 0.001\}$ were added to the exact $\{\tilde{M}_i, \tilde{R}_i\}$ points from the GM1L equation of state to construct data sets with 1000 perturbed $\{M_i, R_i\}$ curves for each of the four error amplitudes.

currently achievable observational error levels, while the smaller values $\mathcal{A} = \{0.01, 0.001\}$ were included to explore how accurately the equation of state might be determined if/when more accurate data become available. Mock observational data collections, each containing 1000 $\{M_i, R_i\}$ noisy mass-radius curves, were constructed for each of these error amplitudes: $\mathcal{A} = \{0.2, 0.1, 0.01, 0.001\}$. Figure 3 illustrates the regions of the mass-radius plane occupied by the points in these four mock observational data collections.

IV. UNCERTAINTY QUANTIFICATION

This section describes the uncertainty quantification analysis of the relativistic inverse stellar structure problem performed for this study. This analysis begins by solving the inverse stellar structure problem outlined in Sec. II for each collection of mock observational data $\{M_i, R_i\}$ described in Sec. III. These solutions provide equations of state for each data set in the collections defined by their error amplitudes, $\mathcal{A} = \{0.2, 0.1, 0.01, 0.001\}$. Evaluating the relationship between the accuracies of these equations of state and the accuracies of the mock observational data used to compute them determines the uncertainty quantification for this problem.

The first step in this analysis is to minimize the differences between the model observables $\{M(p_c^i, v_a), R(p_c^i, v_a)\}$ and the mock observational data $\{M_i, R_i\}$ as measured by the mass-radius fitting function χ defined in Eq. (1). These minimizations have been carried out for this study for each of the mock observational data sets using equation of state

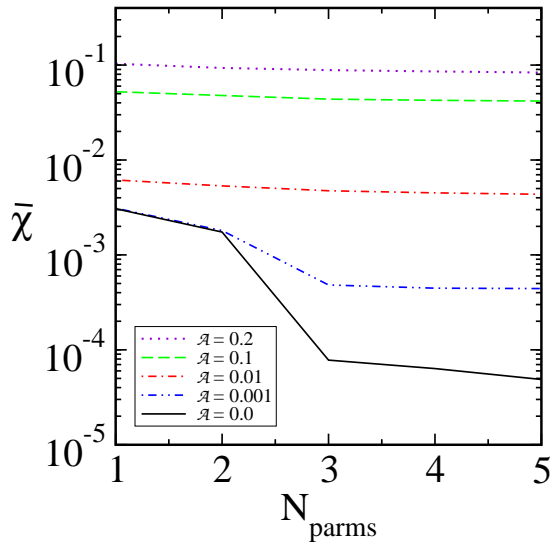


FIG. 4: Values of $\bar{\chi}$, the mass-radius fitting errors defined in Eq. (1) averaged over the collection of mock observational $\{M_i, R_i\}$ data, as functions of N_{parms} , the number of spectral parameters used to model the high density equation of state.

representations with $N_{\text{parms}} = 1, \dots, 5$ spectral parameters. The numerical calculations used in this study were performed using two independent codes to confirm the accuracy of the results. The χ^2 minimizations were carried out numerically using a Fortran implementation of the Levenburg-Marquardt algorithm as described in Ref. [20], and using the `scipy.optimize.least_squares` implementation in Python [21]. The resulting minimal values of χ obtained by these independent codes agree to within a few percent.

Figure 4 illustrates how well the model observables are able to fit the collections of mock noisy data with error amplitudes $\mathcal{A} = \{0.2, 0.1, 0.01, 0.001\}$. The quantity $\bar{\chi}$ is the average of the minimum values of χ over the 1000 $\{M_i, R_i\}$ data sets with error amplitude \mathcal{A} . Figure 4 illustrates $\bar{\chi}$ for each collection of mock data as functions of the number of spectral parameters used to compute the model observables. These results show that these minimum $\bar{\chi}$ values are about half the values of the observational errors for the $\mathcal{A} = \{0.2, 0.1, 0.01\}$ data collections, as well as the $N_{\text{parms}} = 3, \dots, 5$ cases for the $\mathcal{A} = 0.001$ collection. The solid (black) curve in Fig. 4 is the graph of the minimum χ values for the exact reference $\{\tilde{M}_i, \tilde{R}_i\}$ data. These exact results, labeled $\mathcal{A} = 0.0$ in Fig. 4, show that the minimum values of $\bar{\chi}$ for the $N_{\text{parms}} = 1, 2$ cases of the $\mathcal{A} = 0.001$ collection are limited by the accuracy of the spectral representation of the equation of state rather than the accuracy of the observational $\{M_i, R_i\}$ data.

Figure 5 illustrates the range of χ values obtained for each collection of noisy $\{M_i, R_i\}$ data. Note that the upper limits of these χ ranges are smaller than the observational data errors for the $\mathcal{A} = \{0.2, 0.1, 0.01\}$ data collections, and for the $N_{\text{parms}} = 4, 5$ cases of the $\mathcal{A} = 0.001$

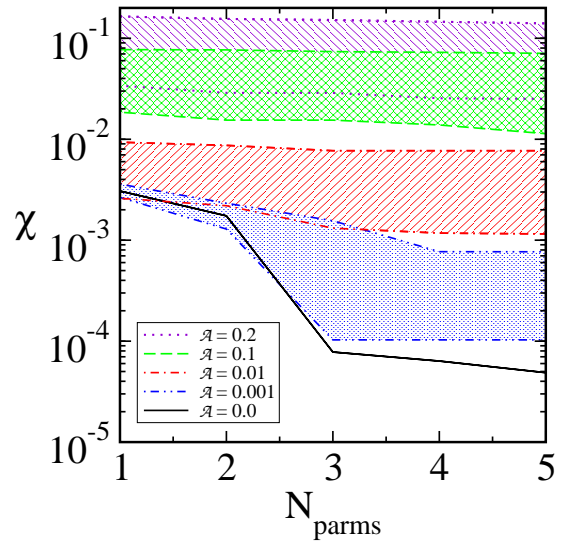


FIG. 5: Ranges of the minimum values of χ , the mass-radius fitting errors defined in Eq. (1), for each collection of mock observational $\{M_i, R_i\}$ data as functions of N_{parms} , the number of spectral parameters used to model the high-density equation of state.

collection. These results show that the neutron-star models constructed here do a good job of representing noisy observational $\{M_i, R_i\}$ data at an accuracy level commensurate with the amplitude of the observational errors.

The next step is to evaluate the accuracy of the equations of state determined by the spectral parameters, v_a , that minimize the mass-radius fitting errors χ . These accuracies are measured by comparing the model equation of state determined by the minimizing parameters, v_a , with the GM1L equation of state used to compute the exact $\{\tilde{M}_i, \tilde{R}_i\}$ data. These comparisons are made by evaluating the equation of state error function Δ defined in Eq. (2) for each $\{M_i, R_i\}$ data set. Figure 6 illustrates $\bar{\Delta}$, the average value of Δ over each of the collections, $\mathcal{A} = \{0.2, 0.1, 0.01, 0.001\}$, along with the results for the exact $\mathcal{A} = 0.0$ case, as functions of the number of spectral parameters, N_{parms} . This figure shows that increasing the number of spectral parameters does not necessarily increase the accuracy of the equation of state determined by the inverse stellar structure problem using noisy mass-radius data. For the $\mathcal{A} = \{0.2, 0.1\}$ collections, the optimal number of spectral parameters is $N_{\text{parms}} = 1$. Observational data with higher accuracies can benefit, however, from higher order spectral representations. The best accuracy for the $\mathcal{A} = 0.01$ collection could perhaps be improved a little over the $N_{\text{parms}} = 1$ case using $N_{\text{parms}} = 3$, and the accuracy for the $\mathcal{A} = 0.001$ collection could definitely be improved over the $N_{\text{parms}} = 1$ case using $N_{\text{parms}} = 4$.

Figure 7 illustrates the range of Δ values obtained for the collections of noisy $\{M_i, R_i\}$ data with $\mathcal{A} = \{0.2, 0.1, 0.01, 0.001\}$ as well as the values obtained for

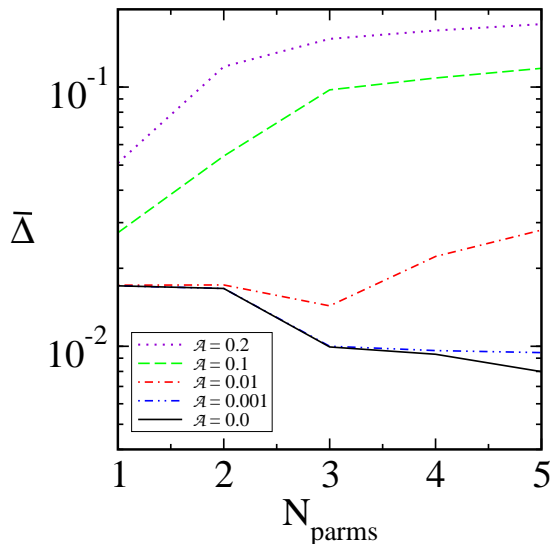


FIG. 6: Equation of state errors $\bar{\Delta}$ averaged over each collection of 1000 $\{M_i, R_i\}$ data sets are shown as functions of the number of spectral parameters N_{parms} . The fitting error Δ is also shown for the equation of state obtained using the exact, $\mathcal{A} = 0.0$, $\{\tilde{M}_i, \tilde{R}_i\}$ data set as the solid (black) curve.

the $\mathcal{A} = 0.0$ case using the exact $\{\tilde{M}_i, \tilde{R}_i\}$ data. Also shown for comparison in Fig. 7 are the values of Δ for the optimal spectral representations of the GM1L equation of state. These optimal representations are obtained by minimizing Δ defined in Eq. (2) with respect to variations in the equation of state parameters v_a [15] using all the points $\{\epsilon_k, p_k\}$ in the table that defines the GM1L equation of state. These optimal values are distinct from and smaller than the values obtained for the $\mathcal{A} = 0.0$ case by minimizing χ using the exact $\{\tilde{M}_i, \tilde{R}_i\}$ data. The upper limits of the ranges of Δ in the $\mathcal{A} = \{0.2, 0.1, 0.01\}$ data collections are smallest for the $N_{\text{parms}} = 1$ spectral representations, showing that this is the best spectral order to use for these cases. These upper range limits show that the equation of state can be determined at an accuracy level commensurate with the size of the observational error using an $N_{\text{parms}} = 1$ spectral representation, unless the observational error is smaller than $\mathcal{A} = 0.01$. The results in Fig. 7 also show that improving the accuracy with which the equation of state can be determined by adding spectral parameters beyond $N_{\text{parms}} = 1$ will not succeed unless the error levels in the observational $\{M_i, R_i\}$ data are at the $\mathcal{A} = 0.001$ level or smaller. It is also interesting to note that the minimum range of the $\mathcal{A} = 0.001$ data in Fig. 7 extend almost all the way to the optimal GM1L values. Therefore some combinations of mass-radius errors provide more accurate solutions to the inverse structure problem than the exact mass-radius data. Unfortunately it is not possible to know a priori what those optimal mass-radius error combinations are for any given equation of state.

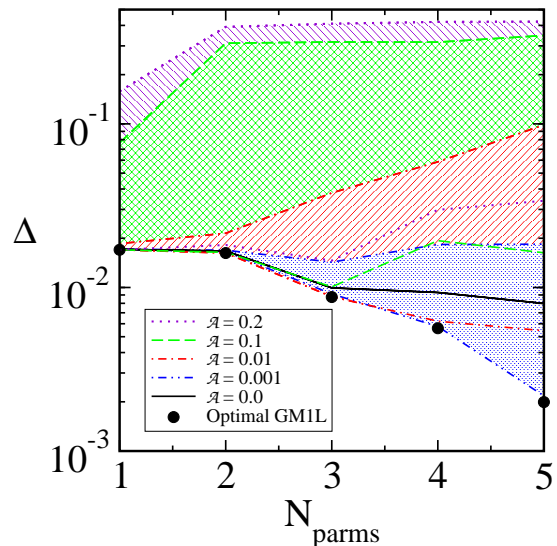


FIG. 7: Ranges of the values of Δ , the equation of state fitting error defined in Eq. (2), for the high density equation of state determined by the best fits for each of the perturbed $\{M_i, R_i\}$ data sets. Also shown as the circular data points is the equation of state error Δ associated with the optimal spectral fit to the exact GM1L equation of state from which the noisy data sets were constructed for this study.

V. DISCUSSION

This study has evaluated the accuracy with which the neutron-star equation of state can be determined by solving the inverse relativistic stellar structure problem using noisy mass and radius data. Large collections of mock observational mass-radius data were prepared by adding random errors with a range of sizes, $\mathcal{A} = \{0.2, 0.1, 0.01, 0.001\}$, to the exact mass-radius values computed from a known neutron-star equation of state. The inverse stellar structure problem was solved using these mock data, and the accuracy of the resulting equations of state were evaluated by comparing them to the nuclear-theory equation of state used to construct the mock mass-radius data. These tests show that in most cases the equation of state can be determined at an accuracy level commensurate with the accuracy of the mass-radius observations. The exceptions to this basic result were for very high accuracy mass-radius data, $\mathcal{A} \leq 0.001$, where the accuracy of the equation of state could be limited by the accuracy of the equation of state representation rather than the accuracy of the mass-radius data.

The method described in Sec. II for solving the relativistic inverse stellar structure problem is simpler than would be required to analyze real observational data. For example, the quantity χ defined in Eq. (1) to measure how well the computed observables $\{M_i(p_c^i, v_a), R_i(p_c^i, v_a)\}$ agree with the observed quantities $\{M_i, R_i\}$ treats each observed quantity equally. The analysis of real $\{M_i, R_i\}$ data, however, should weight each observed quantity in χ individually, so that accurate

measurements contribute more to χ , while those with less accuracy contribute less. The mock data constructed for this study have error distributions of the same size for all the observables in each mock data set. Consequently no observable specific weighting was needed in the definition of the χ measure for this study. Similarly, the errors associated with real $\{M_i, R_i\}$ observations will satisfy complicated probably distributions determined by the particular observational technique. The uniform error distributions used in this study were chosen for their simplicity. Our expectation is that the commensurate relationship between the size of the observational errors and the accuracy of the inferred equation of state found here should apply qualitatively for realistic observational error distributions.

One interesting, and perhaps somewhat counter intuitive, finding of this study is the fact that increasing the number of parameters included in the spectral representation does not in general increase the accuracy of the equation of state determined by the inverse stellar structure problem using noisy mass-radius data. The average equation of state errors, $\bar{\Delta}$, are smallest for the $N_{\text{parms}} = 1$ representations of the noisy mass-radius data with error amplitudes $\mathcal{A} = \{0.2, 0.1\}$. Increasing N_{parms} in these cases produces worse approximations. This non-convergent behavior can occur when attempting to fit noisy data with models having too many parameters.² The exceptions to this general rule are cases with much higher accuracy data, $\mathcal{A} = \{0.01, 0.001\}$. The $\mathcal{A} = 0.01$ case is marginal, but $\bar{\Delta}$ is decreased somewhat by increasing from $N_{\text{parms}} = 1$ to $N_{\text{parms}} = 3$ in this case. The $\mathcal{A} = 0.001$ case is more clear cut; $\bar{\Delta}$ is significantly reduced by increasing from $N_{\text{parms}} = 1$ to $N_{\text{parms}} = 3$ or 4.

The physical neutron-star equation of state is still unknown at this point. Therefore in the analysis of actual mass-radius observations it is not possible to evaluate a direct measure of the accuracy of the inferred equation of state with the Δ measure used here. Consequently it is more difficult in real situations to determine the optimal number of equation of state parameters, N_{parms} , to use for the data analysis. The results of this study, however, suggest a possible way to do this. Consider the N_{parms} dependence of the average mass-radius fitting errors, $\bar{\chi}$, illustrated in Fig. 4. The values of $\bar{\chi}$ in this study are essentially independent of N_{parms} for the $\mathcal{A} = \{0.2, 0.1, 0.01\}$ collections of mock mass-radius

data. Thus the quality of the model fits to those mass-radius data are not significantly improved beyond the $N_{\text{parms}} = 1$ fits. This result is in good agreement with the average accuracies, $\bar{\Delta}$, of the equation of state fits shown in Fig. 6 using those mock data. Only the $\mathcal{A} = 0.001$ curve in Fig. 4 shows a significant improvement in $\bar{\chi}$ at $N_{\text{parms}} = 3$, in good agreement again with the average accuracy $\bar{\Delta}$ obtained for that case. This suggests that the analysis of real mass-radius data should include evaluating the mass-radius fitting errors χ for a range of values of N_{parms} using a convergent representation of the equation of state. This study suggests that the optimal choice of N_{parms} is the point where χ becomes relatively constant for higher values of N_{parms} . Using this approach requires the use of a parametric equation of state representation whose accuracy can be improved by increasing the number of parameters, e.g. those in Refs. [15, 22–24], rather than a representation having a fixed number of parameters like Ref. [25].

Another detail that deserves a little more discussion is the difference between the $\mathcal{A} = 0.0$ results shown in Figs. 4–7, and the optimal GM1L spectral fit shown in Fig. 7. The $\mathcal{A} = 0.0$ results are solutions to the inverse stellar structure problem using the exact $\{\bar{M}_i, \bar{R}_i\}$ data. (The “exact” $\{\bar{M}_i, \bar{R}_i\}$ used here have fractional errors below 10^{-7} .) The $\mathcal{A} = 0.0$ curves in the various figures illustrate how well the inverse structure problem could be solved if observational errors were significantly reduced below present levels. The results for the optimal GM1L spectral fit shown in Fig. 7 represent the accuracy of the spectral fit obtained by minimizing $\Delta(v_a)$ in Eq. (2) with respect to variations in the spectral parameters v_a . The difference between the $\mathcal{A} = 0.0$ and the optimal GM1L curves in Fig. 7 shows that there are (generally small) limitations to the accuracy of the solutions of the inverse structure problem that go beyond the errors in the observational data or the intrinsic accuracy of the spectral representations. These differences might be caused by the limited number of data N_{MR} or the distribution of mass-radius data used in this study.

Appendix A: Causal Spectral Representations

This Appendix summarizes the Chebyshev based causal spectral representations of the high-density neutron-star equations of state used in this study, developed originally in Ref. [15]. These Chebyshev based representations have been shown to provide efficient convergent representations for a wide range of potential neutron-star equations of state, including those with first- and second-order phase transitions.³ The speed of

² Consider the simple case of fitting an exact straight line in two-dimensions using three noisy data points located around this line. Fitting these data with two parameters would produce a line whose location and slope approximate the exact line at some level of accuracy. Using three parameters, however, would produce a parabola that exactly matches the data but could be a much worse model of the exact line. The broad regions occupied by the large error-amplitude noisy mass-radius data in Fig. 3 do not provide enough structure to determine any higher-order spectral parameters beyond $N_{\text{parms}} = 1$ for the $\mathcal{A} = \{0.2, 0.1\}$ data sets.

³ Spectral representations were tested in Ref. [26] for model neutron-star equations of state with a wide range of first- or second-order phase transitions. The range of first-order tran-

sound, v , in a barotropic fluid is determined by the equation of state: $v^2 = dp/d\epsilon$ [27]. These sound speeds are causal if and only if the velocity function Υ ,

$$\Upsilon = \frac{c^2 - v^2}{v^2}, \quad (\text{A1})$$

is non-negative, $\Upsilon \geq 0$, where c is the speed of light.

The velocity function Υ is determined by the equation of state: $\Upsilon(p) = c^2 d\epsilon/dp - 1$. Conversely, $\Upsilon(p)$ can be used as a generating function from which the standard equation of state, $\epsilon = \epsilon(p)$, can be determined by quadrature. The definition of the velocity function $\Upsilon(p)$ can be re-written as the ordinary differential equation,

$$\frac{d\epsilon(p)}{dp} = \frac{1}{c^2} + \frac{\Upsilon(p)}{c^2}. \quad (\text{A2})$$

This equation can then be integrated to determine the equation of state, $\epsilon = \epsilon(p)$:

$$\epsilon(p) = \epsilon_{\min} + \frac{p - p_{\min}}{c^2} + \frac{1}{c^2} \int_{p_{\min}}^p \Upsilon(p') dp'. \quad (\text{A3})$$

Causal parametric representations of the neutron-star equation of state can be constructed by expressing $\Upsilon(p, v_a)$ as a spectral expansion based on Chebyshev polynomials developed in Ref. [15]:

$$\Upsilon(p, v_a) = \Upsilon_{\min} \exp \left\{ \sum_{a=0}^{N_{\text{parms}}-1} v_a (1+y) T_a(y) \right\}, \quad (\text{A4})$$

where the $T_a(y)$ are Chebyshev polynomials. The variable y (defined below) is a function of the pressure having the property that $y = -1$ when $p = p_{\min}$. The constants p_{\min} and Υ_{\min} are evaluated from the low-density equation of state at the point $p = p_{\min}$ where it matches onto the high density spectral representation determined by Eq. (A4). Choosing p_{\min} and Υ_{\min} in this way ensures that no artificial first- or second-order phase-transition discontinuity is introduced at the matching point. These expansions guarantee that $\Upsilon(p) \geq 0$ for every choice of v_a . Therefore any equation of state determined from one of these $\Upsilon(p, v_a)$ automatically satisfies the causality and thermodynamic stability conditions.

Chebyshev polynomials are defined by the recursion relation $T_{a+1}(y) = 2yT_a(y) - T_{a-1}(y)$ with $T_0(y) = 1$ and $T_1(y) = y$. Spectral expansions using Chebyshev basis functions are well behaved on the domain $-1 \leq$

$y \leq 1$ [28]. Therefore the variable y that appears in Eq. (A4) has been defined as

$$y = -1 + 2 \log \left(\frac{p}{p_{\min}} \right) \left[\log \left(\frac{p_{\max}}{p_{\min}} \right) \right]^{-1}, \quad (\text{A5})$$

to ensure that $-1 \leq y \leq 1$ for pressures in the range $p_{\min} \leq p \leq p_{\max}$. The factor $1 + y$ that appears in Eq. (A4) ensures that $\Upsilon(p, v_a)$ has the limit, $\Upsilon(p_{\min}, v_a) = \Upsilon_{\min}$, for every choice of spectral parameters v_a . The values of the equation of state parameters used in this study to model the high-density portion of the GM1L equation of state are $p_{\min} = 1.20788 \times 10^{32}$ erg/cm³, $p_{\max} = 8.87671 \times 10^{35}$ erg/cm³, $\epsilon_{\min} = 5.08587 \times 10^{13}$ g/cm³, and $\Upsilon_{\min} = 277.532$.

Acknowledgments

We thank Fridolin Weber for providing us with the GM1L equation of state table used in this study and L.L. thanks Steve Lewis for numerous conversations concerning this work. This research was supported in part by the National Science Foundation grants 2012857 and 2407545 to the University of California at San Diego, USA. T.Z. was supported by a Haverford College KINSC Summer Scholars fellowship.

sitions extended to the discontinuity large enough to trigger an instability that terminates the contiguous sequence of stable neutron stars. The range of second-order transitions extended to the upper limit set by causality. Lower order spectral representations of equations of state with these first- or second-order phase transitions were shown in Ref. [26] to be more accurate than a non-smooth piecewise-analytic causal representation with the same numbers of adjustable parameters.

-
- [1] F. Özel and P. Freire, *Ann. Rev. Astron. and Astroph.* **54**, 401 (2016).
 - [2] T. E. Riley et al., *Astrophys. J. Lett.* **887**, L21 (2019).
 - [3] M. C. Miller et al., *Astrophys. J. Lett.* **887**, L24 (2019).
 - [4] M. C. Miller et al., *Astrophys. J. Lett.* **918**, L28 (2021).
 - [5] B. Biswas, *Astrophys. J.* **921**, 63 (2021).
 - [6] S. Vinciguerra et al., *Astrophys. J.* **961**, 62 (2024).
 - [7] T. Salmi et al. (2024), arXiv:2406.14466.
 - [8] T. Choudhury et al., *Astrophys. J. Lett.* (2024), arXiv:2407.06789.
 - [9] K. Chatziioannou et al. (2024), arXiv:2407.11153.
 - [10] L. Lindblom, *Astrophys. J.* **398**, 569 (1992).
 - [11] R. C. Smith, *Uncertainty Quantification: Theory, Implementation, and Applications*, Computational Science and Engineering (SIAM, 2014).
 - [12] L. Lindblom and N. M. Indik, *Phys. Rev. D* **86**, 084003 (2012).
 - [13] L. Lindblom and N. M. Indik, *Phys. Rev. D* **89**, 064003 (2014).
 - [14] L. Lindblom, *AIP Conference Proceedings* **1577**, 153 (2014).
 - [15] L. Lindblom and T. Zhou, *Phys. Rev. D* **110**, 083030 (2024).
 - [16] W. M. Spinella, Ph.D. thesis, Claremont Graduate University & San Diego State University (2017).
 - [17] N. K. Glendenning and S. A. Moszkowski, *Physical Review Letters* **67**, 2414 (1991).
 - [18] S. Typel, G. Röpke, T. Klähn, D. Blaschke, and H. H. Wolter, *Physical Review C* **81**, 015803 (2010).
 - [19] J. R. Oppenheimer and G. M. Volkoff, *Phys. Rev.* **55**, 374 (1939).
 - [20] W. H. Press, S. A. Teukolsky, W. T. Vetterling, and B. P. Flannery, *Numerical Recipes in FORTRAN* (Cambridge University Press, Cambridge, England, 1992), 2nd ed.
 - [21] P. Virtanen, R. Gommers, T. E. Oliphant, M. Haberland, T. Reddy, D. Cournapeau, E. Burovski, P. Peterson, W. Weckesser, J. Bright, et al., *Nature Methods* **17**, 261 (2020).
 - [22] L. Lindblom, *Phys. Rev. D* **82**, 103011 (2010).
 - [23] L. Lindblom, *Phys. Rev. D* **97**, 123019 (2018).
 - [24] L. Lindblom, *Phys. Rev. D* **105**, 063031 (2022).
 - [25] J. S. Read, B. D. Lackey, B. J. Owen, and J. L. Friedman, *Phys. Rev.* **D79**, 124032 (2009).
 - [26] L. Lindblom, *Phys. Rev. D* **110**, 043018 (2024).
 - [27] L. D. Landau and E. M. Lifshitz, *Fluid Mechanics* (Pergamon Press, 1959).
 - [28] J. P. Boyd, *Chebyshev and Fourier Spectral Methods* (Dover Publications, 1999), 2nd ed.